International Journal of Heat and Mass Transfer 251 (2025) 127351

Contents lists available at ScienceDirect

International Journal of Heat and Mass Transfer

journal homepage: www.elsevier.com/locate/ijhmt

Reduced-order-driven recurrent neural network for ultra-fast thermal field simulation in high-heat-flux electronic systems

Linyi Xiang [a,1], Fengjun Wang [a,b,1], Yuntao Zha [a], Yupeng Hu [b], Bisheng Zhang [a], Xuan Yang [a], Run Hu [a], Xiaobing Luo [a,*]

[a] School of Energy and Power Engineering, Huazhong University of Science and Technology, Wuhan 430074, China
[b] Institute of systems Engineering, China Academy of Engineering Physics, Mianyang 621999, China

ARTICLE INFO

Keywords:
Reduced order model
Proper orthogonal decomposition
Neural networks
Thermal field simulation
Spray cooling

ABSTRACT

Thermal overloading represents a primary contributor to electronic system failures, underscoring the critical importance of real-time thermal monitoring, prediction, and field reconstruction. While conventional full-order simulation methods demand substantial computational resources, our work addresses this challenge through an innovative POD-machine learning hybrid framework designed for temporally evolving temperature field prediction in high-heat-flux electronic systems. By integrating LSTM and BiLSTM, we have enhanced and accelerated the traditional POD-Galerkin strategy. The framework demonstrates superior predictive capability, achieving maximum RMSE values below 0.1 for POD mode coefficients across eight spray cooling system operating conditions with ten POD mode coefficients. Through two different transfer learning strategies implementation, we have realized significant improvements in computational efficiency, reducing prediction time to 7.8 s for complex temperature fields spanning 2000 s. The synergistic integration of POD's physical interpretability and machine-learning's nonlinear prediction capabilities establishes a robust framework with considerable potential for diverse applications in bio-inspired robotics, energy production, thermal management systems, and big data analytics.

1. Introduction

Motivated by the growing trend towards integration and miniaturization in advanced electronics, the performance of thermal management and monitoring systems has become increasingly critical, especially in high heat-flux scenarios [1,2]. The exponentially rising heat flux can destroy the high-integration electronics [3,4]. Consequently, the design of effective thermal management system, along with the accurate reconstruction and prediction of temperature fields, play crucial roles for the electronic system safety and maintenance [5,6]. From the dawn of industrialization to the present, achieving the above objectives has typically relied on direct measurement and conventional full-order methods, such as Large Eddy Simulation (LES) and Direct Numerical Simulation (DNS), are usually used [7]. However, it is stressful to obtain accurate and comprehensive temperature field rapidly when dealing with the spatiotemporal complexity of applications due to the large-scale physical equations to be solved and the huge amount of grid [8,9].

Data-driven approaches, such as reduced-order methods (ROMs) and machine learning (ML), are born for the computational bottlenecks by uncovering underlying patterns in data [10,11]. ROMs and ML have superior adaptability and expandability compared to traditional DNS methods [12]. ROMs will demonstrate the origin high-dimensional system by the extracted low-dimensional system at a fraction of the computational cost, such as proper orthogonal decomposition (POD) and dynamic mode decomposition (DMD). The mathematical optimality of POD modes makes POD famous in model reduction method and POD has shown great data analysis capability and condition predictions for both flow field [13,14] and thermal field [15–17]. Over the past decades, researchers dedicated to extending POD to the field of temporal predictions [18]. This inevitably requires solving the physical equations and the most commonly used modeling approach is Galerkin projection (GP) [19,20]. Galerkin projection can achieve the order-reduction of physical equations and it will reduce the degrees of freedom. However,

* Corresponding author.
E-mail address: Luoxb@hust.edu.cn (X. Luo).
[1] These authors contributed equally: Linyi Xiang, Fengjun Wang.

https://doi.org/10.1016/j.ijheatmasstransfer.2025.127351
Received 9 February 2025; Received in revised form 24 May 2025; Accepted 30 May 2025
Available online 4 June 2025

GP exhibits unstable behaviors when encounter non-linear interactions [21,22]. There is another challenge for temporal predictions in POD, namely the extensive iterations required within the grids. Such a dilemma exists particularly when complex geometrical models and boundary conditions are involved. Importantly, these shortcomings reflect one of the most prominent advantages of POD-Galerkin, namely physical interpretability, which is not the case with machine learning [23,24]. ML is a black-box model without physical basis while it is strong in nonlinearity because of the nonintrusive treatment means. Based on various machine learning algorithms, ML has shown promising results in weather forecasting [25], image recognition [26], and thermoregulation [27]. It is worthy pointing out that some researchers established the low-dimensional methods based on ML such as convolution neural networks (CNN) which is also called reduced-order methods [28,29]. However, these approaches differ fundamentally from POD in their underlying principles. In terms of temporal predictions, recurrent neural networks (RNN) have proven effective for short-term sequence forecasting [30,31]. Yet, when it is necessary to analyze and predict the behavior of a dataset over a longer period of time, RNN is prone to the problem of vanishing gradients [32]. A dataset over a longer period of time usually contains significant amount of time series data which exhibit high dimensionality and complex interdependencies. Long short-term memory neural network (LSTM) is one of the variants of RNN which avoids the vanishing gradient [33]. LSTM can learn complicated temporal dependencies and capture long-term trends in the dataset which has been proven in electricity consumption [34], load forecasting [35], and carbon neutral [36]. Furthermore, in order to capture bidirectional relationships within time series data, the Bidirectional long short-term memory neural network (BiLSTM) is proposed [37,38]. The prior information on the governing equations of POD-Galerkin and the powerful analytical ability for non-linear problems of ML make it possible to combine the above two methods for a more stable and accurate algorithm in the temporal prediction. San et al. [39] stabilized POD by ANN and predicted the modal eddy viscosity coefficient for turbulent geophysical flows which is robust for larger choices of time steps. Wang et al. [40] investigated the ocean gyre and flow past a cylinder by combining the POD with LSTM to predict the POD mode coefficient. Yousif et al. [41] compared the performance of LSTM and BiLSTM in predicting the POD mode coefficients of turbulent flow around a finite wall-mounted square cylinder and BiLSTM shows superior results. Mohan et al. [42] examined the LSTM and BiLSTM for turbulent flow prediction in POD mode coefficients. Although the LSTM and BiLSTM have been proven to be effective by incorporating with POD in flow field, it remains relatively unexplored for the application in the thermal field prediction with spatiotemporal complexity. The partial differential equations (PDEs) of the flow field are Navier-Stokes equations and the heat conduction, convection, and radiation equations for thermal field. The thermal management system of electronics is a proper candidate for this attempt which is a highly non-linear system and there is an urgent need for fast simulation and design [43].

In this work, we develop a reduced-order-driven recurrent neural network for thermal field reconstruction and prediction using LSTM and BiLSTM by combining the POD method. In particular, the core strengths of POD and machine learning are integrated. The transfer learning (TL) is introduced into the approach for improving the robustness and adaptability of the proposed method. We choose one of the most prominent thermal management technologies for validation, namely spray cooling [7]. The temperature field of the electronic system with high heat flux in spray cooling is reconstructed and predicted. For assessing the proposed method, we utilize the root mean square error (RMSE) and R-squared (R^2).

The remainder of this paper is organized as follows. Section 2 gives the methods and experiment setup, especially the mathematical formulations used in this work. The performance of the proposed reduced-order method based on different ML algorithms are illustrated in Section 3. Finally, in Section 4, discussion, conclusions, and the potential application of our method are provided.

2. Methods and experiment setup

2.1. Proper orthogonal decomposition

As a reduced-order method, proper orthogonal decomposition (POD) is a method derived from the statistical analysis of vector data. POD achieves a significant reduction in the amount of data required to analyze the original system by extracting the main "features" of the system. Here, the "features" means the POD modes and POD mode coefficients. In this work, the original system refers to the temperature field of spray cooling module and we assemble the temperature data into a matrix T(x,t). By POD, the T(x,t) is

$$T(x,t) = \sum_{i=1}^{\infty} \varphi_i(x)\alpha_i(t)$$

An approximate temperature matrix T'(x,t) can be expressed as

$$T'(x,t) = \sum_{i=1}^{n} \varphi_i(x)\alpha_i(t)$$

The $\varphi_i(x)$ refers to the POD mode, $\alpha_i(t)$ denotes the POD mode coefficient, and n denotes the number of POD mode. The selection of POD mode depends on the amount of energy and will be described in more detail below.

It's worth noting that POD modes will not change with the time while they are a set of the optimal mutually orthogonal bases:

$$(\varphi_i, \varphi_j) = \delta_{ij} = \begin{cases} 0 & i \neq j \\ 1 & i = j \end{cases}$$

Therefore, our goal in training and forecasting on time sequence is POD mode coefficients.

2.2. Long short-term memory neural network

As discussed before, the Long short-term memory neural network (LSTM) is one of the variants of recurrent neural networks (RNN) which overcomes the stability bottlenecks such as vanishing gradient. Benefit from its unique framework, as shown in Fig. 1(a), LSTM has shown excellent forecasting capacity in time series problems. The framework of LSTM cell contains three gates: the input gate, output gate, and the forget gate, representing by i, o, and f, respectively. The cell input is given by x and the cell output is denoted as L, while t is the step of the sequential data which is used to express the temporal ordering of data. The input gate will decide the selectively adding information into the LSTM cell and the output information L is controlled by output gate. The key gate in LSTM is the forget gate, which is employed to discard some information for reducing over-fitting. In each LSTM cell, the equations for computing the gates are as follows:

$$i_t = \sigma(W_i x_t + U_i L_{t-1} + b_i)$$

$$f_t = \sigma\left(W_f x_t + U_f L_{t-1} + b_f\right)$$

$$\widetilde{C}_t = \tanh(W_C x_t + U_C L_{t-1} + b_C)$$

$$C_t = i_t \otimes \widetilde{C}_t + f_t \otimes C_{t-1}$$

$$o_t = \sigma(W_o x_t + U_o L_{t-1} + b_o)$$

$$L_t = o_t \otimes \tanh(C_t)$$

Where the arithmetic of σ and tanh are

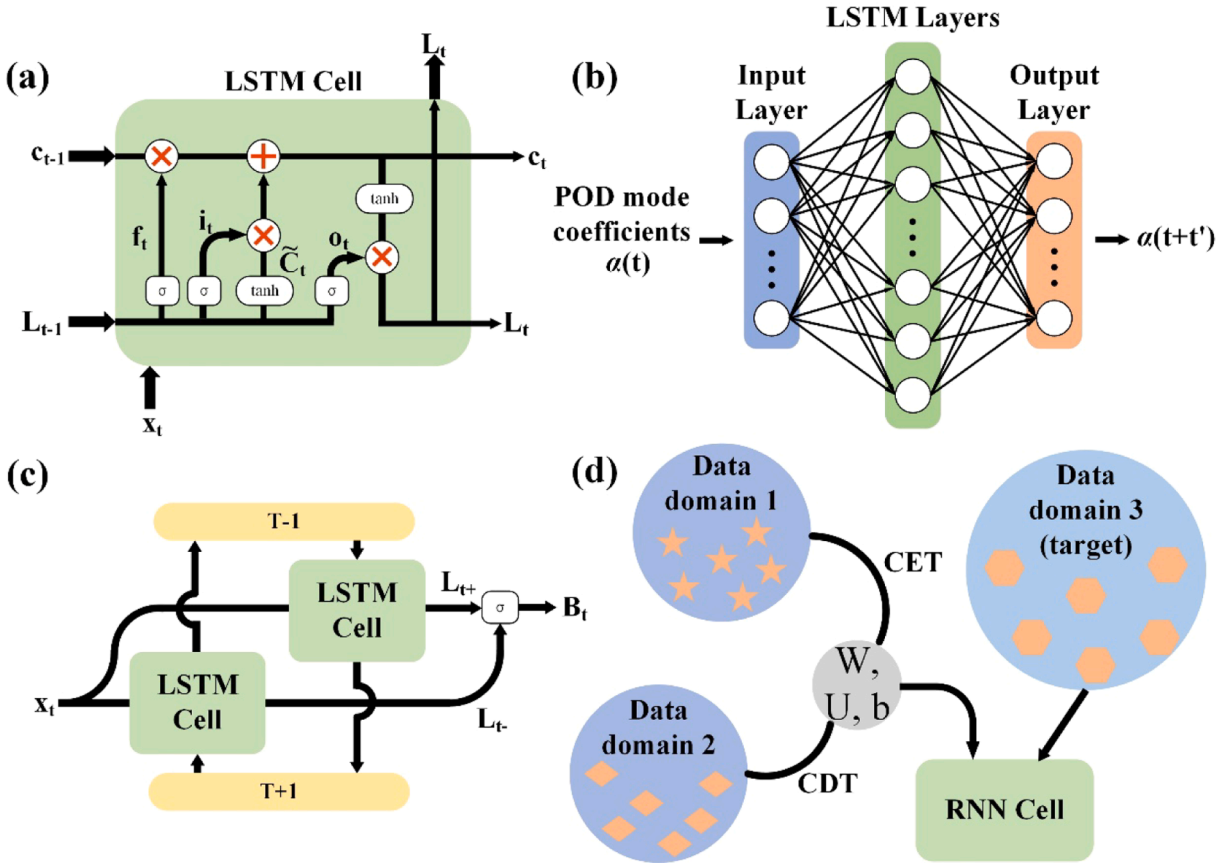

Fig. 1. The architecture of different methods. (a) LSTM cell. (b) The schematic diagram of LSTM layer. (c) BiLSTM. (d) Transfer learning.

$$\sigma(x) = \frac{1}{1+e^{-x}}$$

$$\tanh(x) = \frac{\sinh(x)}{\cosh(x)} = \frac{e^{x}-e^{-x}}{e^{x}+e^{-x}}$$

The W and U are the weights for each gate and the b represents the bias value. The cell state is represented as C.

The combination of gates and cell state is the ingenious design for solving the vanishing gradient and expanding the memory. The chain rule is used to compute the weight corrections in the back-propagation algorithm, as a result the small gradients behind restrict the rate of learning of earlier layers. For long prediction sequences, the gradient will gradually vanish, preventing the further learning, namely vanishing gradients. The LSTM cell will trap the gradient and capture the important information. The cell saves them over a long period of time while the abandoned information is determined by the assigned weight value. Therefore, the data predictions are conditional on the recent context in the input sequence, not what has just been presented as the current input to the cell. In Fig. 1(b), the learning architecture of LSTM used in this work is shown. The cyclic connections of cells in the architecture makes it a powerful learning capability. The architecture contains three parts including input layer, LSTM layer (hidden layer), and output layer. Each of cell in hidden layer works as shown in Fig. 1(a). Moreover, the input data are the POD mode coefficients at the moment of t while the output data are the POD mode coefficients at the moment of t + t'.

The Bidirectional long short-term memory neural network (BiLSTM) is a variant of the LSTM. The input data is trained for twice in BiLSTM as shown in Fig. 1(c). In the first cycle, the LSTM cell is used for the forward training while it is used for the backward training in the second cycle. As a result, the double-trained input information can be combined into an output with higher accuracy. Fig. 1(c) illustrates the algorithm for BiLSTM at time t, while T - 1 and T + 1 represent the algorithm for BiLSTM before and after.

2.3. Transfer learning

Modern engineering systems are often characterized by complex structures, variable working and operating conditions. Modelling and training for each situation individually is unwise and cumbersome, especially if there is limited high-quality data. Transfer learning (TL) is a method which can pre-train the neural network model and apply the pre-trained parameters and features to another neural network model for different case. Usually, the pre-trained parameters are weights and bias value in LSTM and BiLSTM. This will greatly reduce the consumption of calculation resources and improve the accuracy.

In this work, we proposed two different TL strategies, coefficient transferring (CET) and condition transferring (CDT). As shown in Fig. 1 (d), based on the data from domain 1 and domain 2, we pre-trained the weights (W, U) and bias value (b) and transfer them to the new RNN cell with data from domain 3. Following the definition of TL, some model parameters should be shared. As a consequence, considering the POD architecture and spray cooling thermal field presented in this paper, we choose POD mode coefficient and spray cooling condition for sharing in TL. To be more specific, in CET, we train the neural network for a POD mode coefficient and extract the weights and bias value for other POD mode coefficients as the initial values of neural networks. In CDT, all of the ten POD mode coefficients are trained in a spray cooling condition case and the optimized weights and bias value will be transferred to other spray cooling condition cases.

2.4. Methodology

The POD, RNNs, and the experiments are coupled for constructing

the model for training and predicting the temperature field of spray cooling in this work. In order to establish the sophisticated three-dimensional spray cooling module and obtain the snapshots, the finite volume method (FVM) is employed. We develop the unstructured grid FVM for POD to deal with the complex boundary conditions. It is worth noting that the whole three-dimensional temperature field is calculated while most of the previous studies have only selected a few slices to analyses. The thermophysical parameters of materials used in the simulation are displayed as below.

In this study, the temperature datasets for 0–1000 s of different cases are obtained by FVM for POD decomposition to obtain the POD modes and mode coefficients. The resulting POD mode coefficient dataset, containing 1000 s temporal resolution, is partitioned into training (80 %) and testing (20 %) subsets for machine learning applications. After the sensitivity analysis, the learning rate, the dropout rate, and the number of hidden layer cells are chosen as 0.001, 0.2, and 2000, respectively. In addition to this, the optimizer is set as Adam, the epochs are 300, and the batch size is 64 in the LSTM/BiLSTM model.

As shown in Fig. 2. the detailed procedures of the proposed framework are summarized as following:

1. The snapshots of the spray cooling temperature field are obtained by FVM. The snapshots will be assembled into a temperature matrix in accordance with time.
2. The temperature matrix will be decomposed through POD, as demonstrated in Section 2.1. The POD mode coefficients obtained from the decomposition will be used to form the datasets for training.
3. The POD mode coefficients are trained by LSTM, BiLSTM, LSTM-TL, and BiLSTM-TL respectively. The trained model will predict the POD mode coefficients of the future.
4. The validation and modification will be constructed based on test data and experiments.
5. The predicted POD mode coefficients is then used for reconstruction of temperature field by combining with the POD modes.

For efficiency and accuracy in training process, the datasets of POD mode coefficients are normalized as

$$x(t) = \frac{\alpha(t) - \alpha(t)_{\min}}{\alpha(t)_{\max} - \alpha(t)_{\min}}$$

The root mean square error (RMSE) and R-squared (R^2) are used for model evaluation, and the computing formula are

$$RMSE = \sqrt{\frac{1}{N}\sum_{i=1}^{N}(y_i - \hat{y}_i)^2}$$

$$R^2 = 1 - \frac{\sum_{i=1}^{N}(y_i - \hat{y}_i)^2}{\sum_{i=1}^{N}(y_i - \bar{y})^2}$$

Where y_i, $\hat{y}_i$, N denotes to the actual value of POD mode coefficient, predicated value of POD mode coefficient, and the total number of observations.

2.5. Spray cooling experiment

The active liquid-cooling technology has the advantages of strong heat dissipation ability, long thermal transport distances, and flexible scenario adaptation. Spray cooling is a promising active liquid-cooling thermal management method for high-heat-flux equipment which is famous for secondary nucleation and preventing wall temperature excursion. In this work, the reason why we choose spray cooling temperature field as the target is not only the wide application prospects of spray cooling, but also the complex heat transfer mechanisms and modelling structures. Our algorithm can be extended to various fields while it is demonstrated in spray cooling successfully.

The experiment setup is shown in Fig. 3. The spray cooling system contains three sub-systems including spray module, electronic system module, and monitoring module. Three thermocouples are embedded into the electronic system for temperature data collection as shown in Fig. 3(c). In each working condition, the temperature fluctuation of the three temperature measurement points will be controlled less than 0.1 °C before proceeding to the next set of experiments, and the experiments will be repeated three times. The dataset in this paper is mainly obtained from previous research [7], due to the aim of training and validation.

3. Results and discussion

The reduced-order-driven recurrent neural network proposed in this

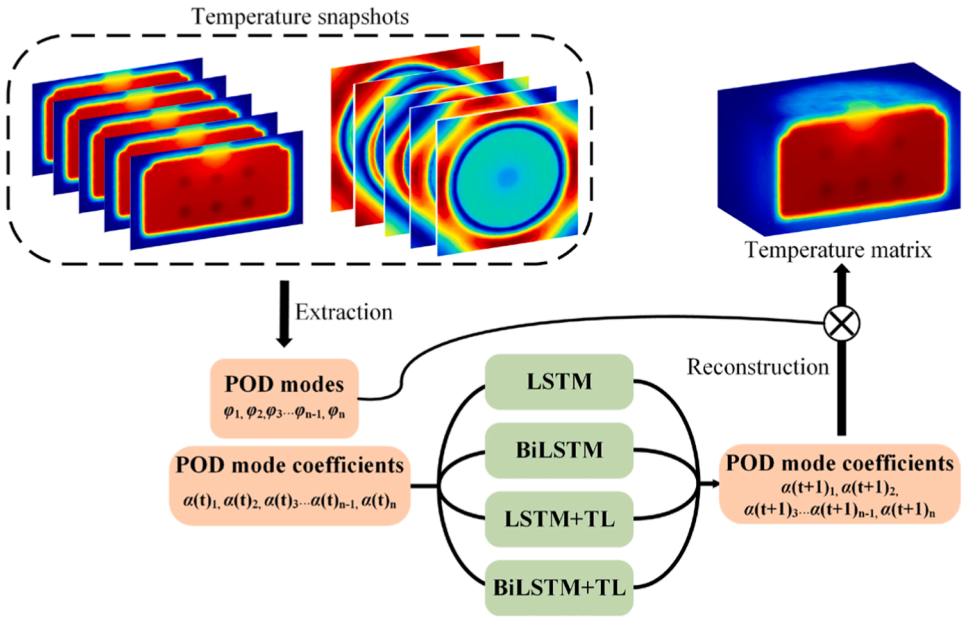

Fig. 2. The schematic of proposed reduced-order-driven recurrent neural network.

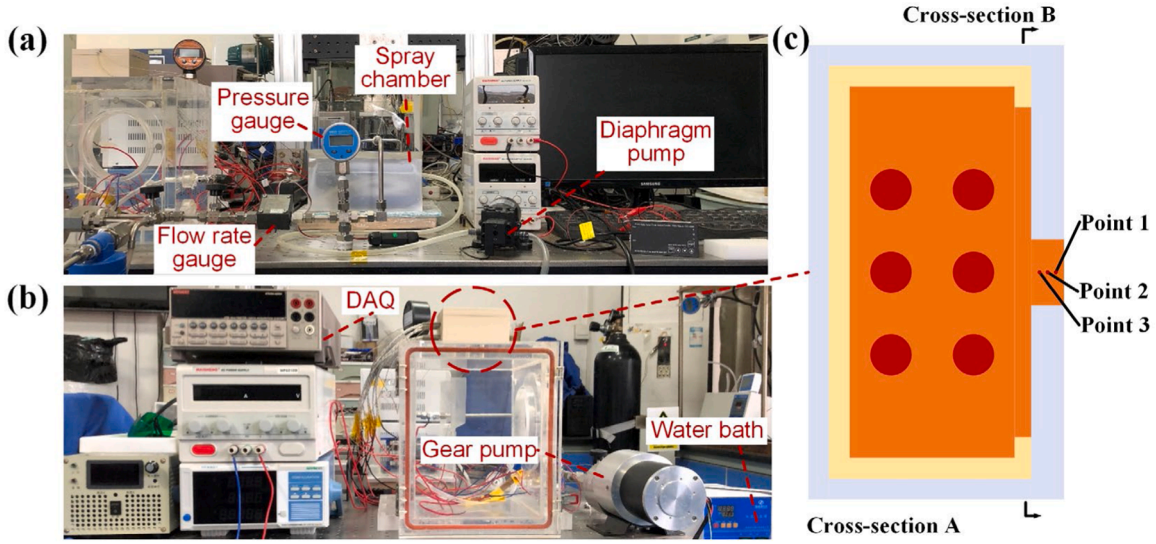

Fig. 3. Spray cooling system. (a) Front view of the experimental system. (b) Side view of the experimental system. (c) Schematic diagram of electronic system.

work are tested for robustness and adaptability based on different cases. The experiments are used to modify and validate the algorithm. In the high-heat-flux electronic system, the primary factors to be considered in a spray cooling thermal management system is the spray volumetric flux, nozzle-to-surface distance, and coolant inlet temperature, which are closely related to the application requirements. in view of this, the chosen cases are listed in the Table 2.

All the simulations are conducted under the same system hardware condition. The processor is Intel(R) Xeon(R) CPU E5–2690 v4 @2.60Ghz 2.60Ghz (Double processors), and the RAM is 64.0GB, and the graphics card is NVIDIA Quadro P2000.

3.1. The performance of POD in temperature field simulation

As previously discussed, the prediction of the temperature field is accomplished through a two-step process: POD and machine learning. In this study, the training datasets consist of POD mode coefficients, making their characteristics crucial for the performance of the proposed algorithm. To illustrate this, case O is utilized as a demonstration. The greater the number of POD modes, the more accurate the calculated temperature field will be. Accordingly, the computational cost will increase. Fortunately, in the first few orders of modes, the accumulated energy is already close to 100 % which means the whole system can be reconstructed accurately. For instance, the Fig. 4 gives out the energy of the POD modes of case O. We choose 10 POD modes and mode coefficients for further training according to the accumulated energy,

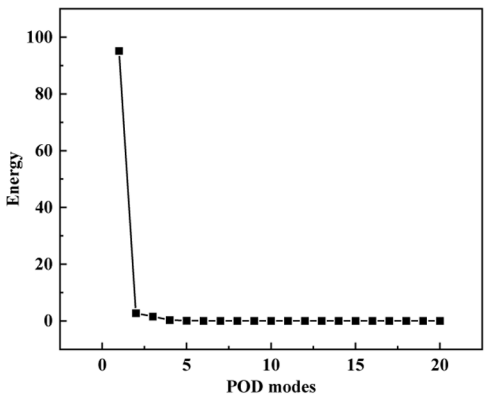

Fig. 4. The energy of different POD modes for case O.

namely $n = 10$. The POD mode coefficients come from the temperature solution of FVM.

The relationship between POD mode coefficients and time are illustrated in Fig. 5(a) and the trend of the evolution of the mode coefficients is not the same in different modes. In order to figure out the optimal mode sets in this case, the number of 1, 3, 5, and 10 POD modes are selected for the temperature field simulation. Fig. 5(b) shows the three-dimensional temperature field error of cross-section A based on four different mode sets from top to bottom, and Fig. 5(c) shows the temperature field error of cross-section B. The benchmark is the FVM standard solution and the temperature field at 2000 s is used for comparison. Although the energy of mode 1 is 95.16 %, the temperature error is more than 14 °C in the bottom area of the module. With the increase of the modes including in the mode set, the temperature field error decreases. Based on the balance of computational resources and accuracy, we chose a mode set containing 5 POD modes for thermal field simulations while the accumulated energy has exceeded 99.9 % and the value of temperature error is on the order of 10^{-1}. It's worth noting that the simulation errors tend to appear at the boundary of the model. This is due to the characteristics of the POD, where the initial few POD modes focus on capturing the main trends in the physical field, such as the regions where large changes in temperature occur. High order modes are constantly correcting the simulation results at the boundary with small temperature changes, which is also matched by the magnitude of the values of the mode coefficients. The wavelength variation of the mode coefficients on time scales is also more complex because corrections made by the higher order mode to the physical field are more refined. This poses a challenge for both the calculation and prediction of POD mode coefficients.

3.2. Prediction of POD mode coefficients based on different methods

The traditional method for obtaining the POD mode coefficients is the temperature field extraction while it requires all the temperature field calculation for each time step. Despite the GP can achieve the extrapolation of POD mode coefficient, the unstable behaviors and the huge iterations within the grids make the prediction of the POD mode coefficient difficult. Therefore, we predict the POD mode coefficient by LSTM and BiLSTM. The physical interpretability of POD method reflects to some extent in the values of the mode coefficients and waveforms. Fig. 6 shows the predicted POD mode coefficients of different POD modes based on four methods for case O. The POD mode coefficients of 0–2000 s are calculated, where the data of 0–1000 s is already known

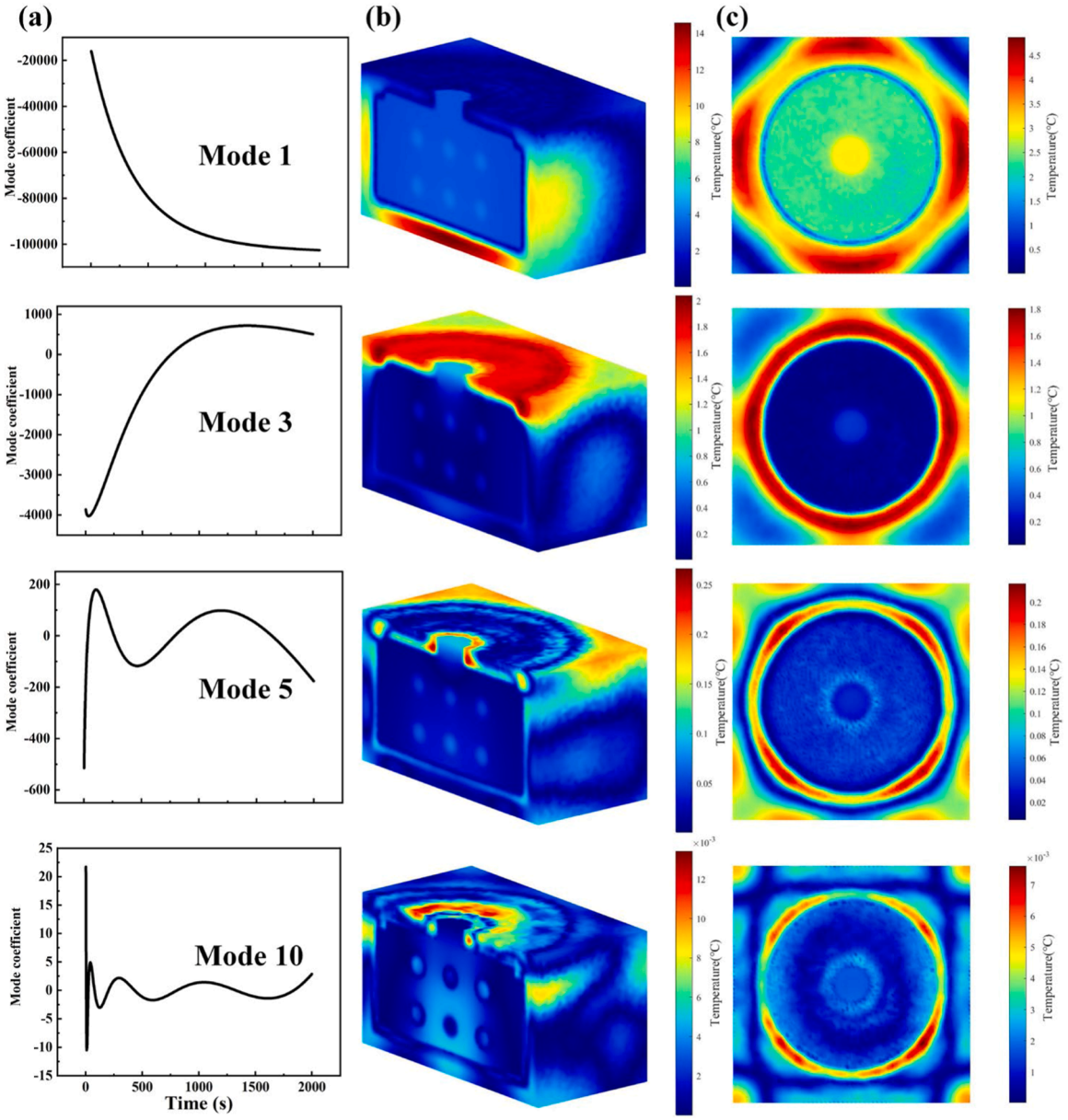

Fig. 5. Illustration of POD modes. (a) POD mode coefficients versus time. (b) Side view of temperature error for cross-section A. (c) Plot of temperature error for cross-section B.

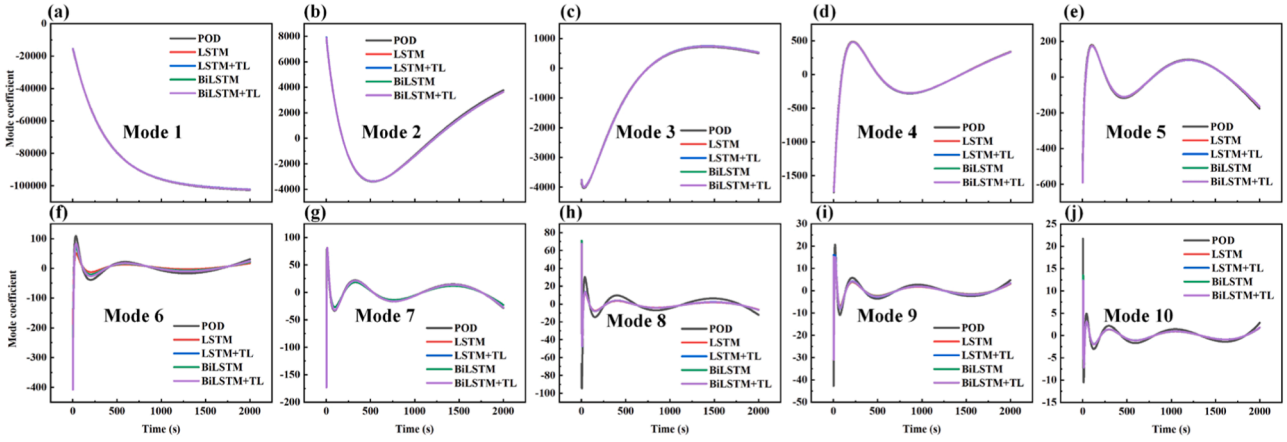

Fig. 6. POD mode coefficients versus the time. (a-j) Different POD modes.

and the data of 1001–2000 s is unknown. The prediction results allow for simultaneous validation both in and out of the sample space.

The POD mode coefficients corresponding to different POD modes show different values and waveforms which reflect the characteristics of the temperature field. Generally speaking, the values of POD mode coefficients decrease as the mode order get higher and the waveforms become progressively more complex. The number of peaks and troughs has been increasing. What's more, the mode coefficients all have an oscillatory regression over time, starting with the largest values at the beginning and gradually diminishing to oscillate around a mean value of zero. This oscillatory behavior introduces additional challenges for machine learning predictions. In low-order modes, the prediction results fit well with the extracted POD mode coefficients for all four methods as shown in Fig. 6(a-e). Deviations appear gradually from mode 6 onwards, but a consistent waveform trend is still achieved. From this, it can be concluded that LSTM, BiLSTM, LSTM+TL, and BiLSTM +TL have a strong ability to predict mode coefficients on time scale. Even though the curves have large fluctuations and variations of values, the prediction results of the methods are still in good agreement with the original POD system. Also, the results show that the excellent prediction accuracy can promise the first five orders of modes for subsequent analyses which is consistent with the conclusions of energy in Section 3.1. In the next section, the differences in the details of the prediction results of the four methods will be described.

3.3. Prediction of temperature field based on different methods

Each of the four methods are used to calculate the temperature field of 0–2000 s. The three-dimensional and two-dimensional temperature fields at two critical time points at the beginning and end of heating are selected for comparison as shown in Fig. 7. The conclusion can be given from the overall temperature field, all four methods have presented the main features and trends of the temperature field. Next, the temperature errors will be analyzed and compared with the experiments.

The high-heat-flux electronic system is experimentally tested and the temperature of three critical points are measured by thermocouples as shown in Fig. 3(c). Fig. 8 and Fig. 9 presents the temperature data and figure predicted by four machine learning methods. The predicted results have a good agreement with the traditional FVM method and the experiments in all three points. The experiments have higher temperature than simulations while it has a consistent trend, and the maximum temperature error is 9.53 °C, about 6.51 % based on LSTM. The situation with BiLSTM is similar and the maximum temperature error is 9.36 °C, about 6.38 %. Simulation comparisons have a better agreement to experiments. The maximum temperature error between FVM and LSTM is 1.12 °C, about 4.34 % while it is 0.98 °C and 3.82 % for BiLSTM. Compared to LSTM, the BiLSTM shows an improvement in the temperature prediction benefiting from bidirectional traversal. This will be more effective in the problems with complex physical mechanism.

The transfer learning (TL) is introduced for further optimization. We pre-train the weights (W, U) and bias value (b) from case O for other cases, namely CDT. The first POD mode is the benchmark for pre-training for other POD modes inside case O, namely CET. As shown in Fig. 9, the TL brings better results for temperature field prediction than LSTM and BiLSTM. Consistent with previous observations, the experimental temperatures are slightly higher than the simulated values. The maximum temperature error for LSTM+TL is 9.55 °C, representing a 6.52 % deviation, while for BiLSTM+TL, they are 9.36 °C and 6.39 %. Simulation comparisons have a better agreement to experiments. The maximum temperature error between FVM and LSTM+TL is 1.15 °C (4.48 %), while it is 0.95 °C (3.73 %) for BiLSTM+TL. The improvement made by TL of the accuracy in maximum temperature error is limited.

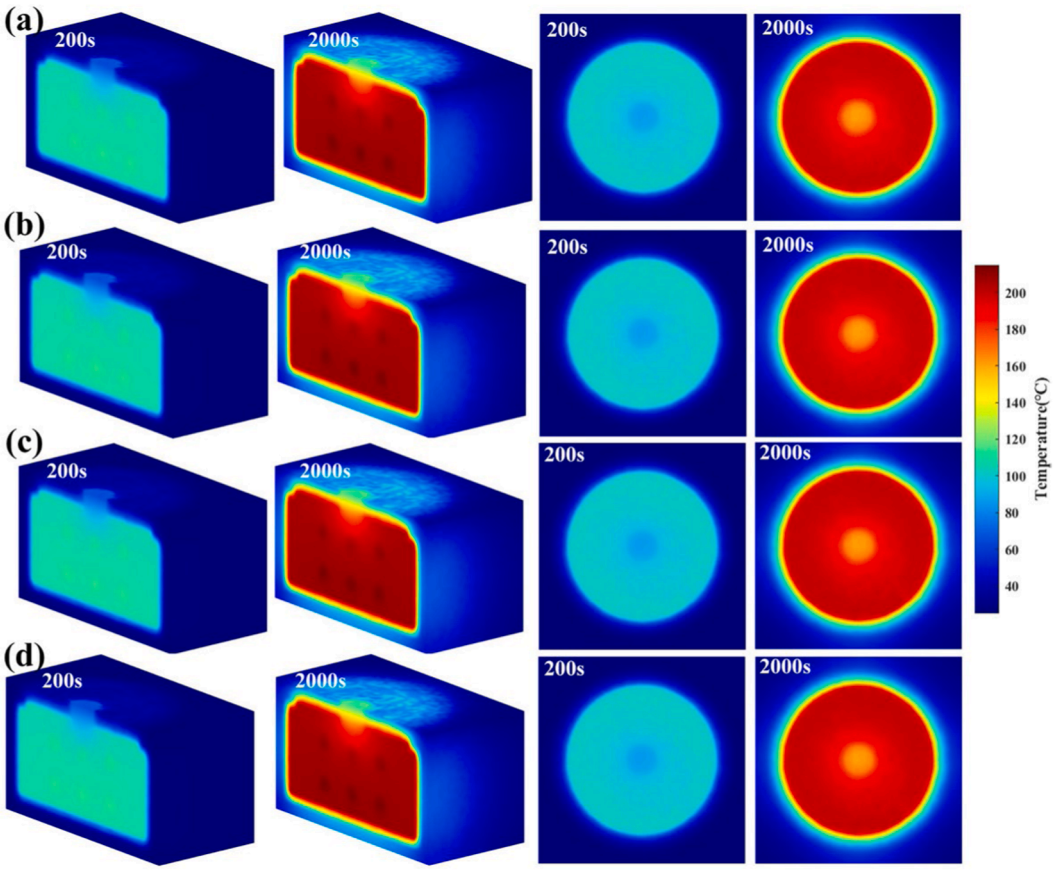

Fig. 7. The predicted temperature field based on different methods at 200 s and 2000 s. (a) LSTM. (b) LSTM+TL. (c) BiLSTM. (d) BiLSTM+TL.

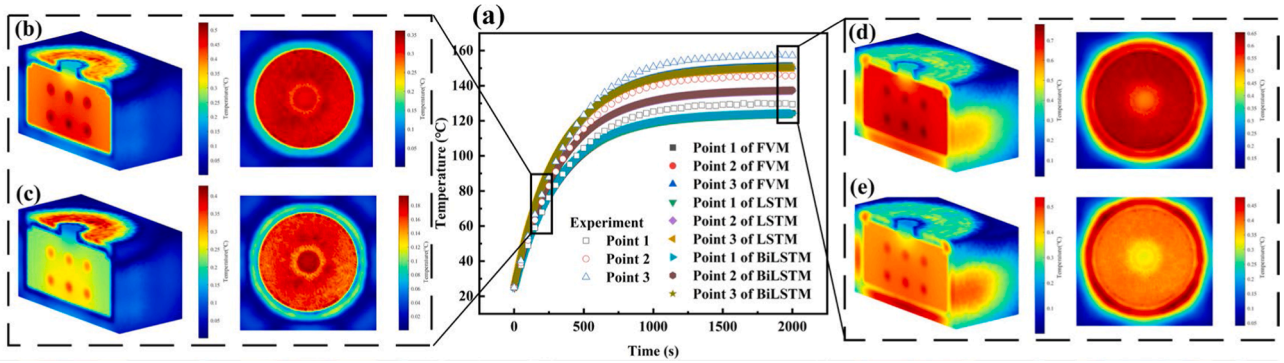

Fig. 8. The predicted temperature based on LSTM and BiLSTM. (a) The experiment and simulation temperature of three critical points versus time. (b) The temperature error of LSTM at 200 s. (c) The temperature error of BiLSTM at 200 s. (d) The temperature error of LSTM at 2000 s. (e) The temperature error of BiLSTM at 2000 s.

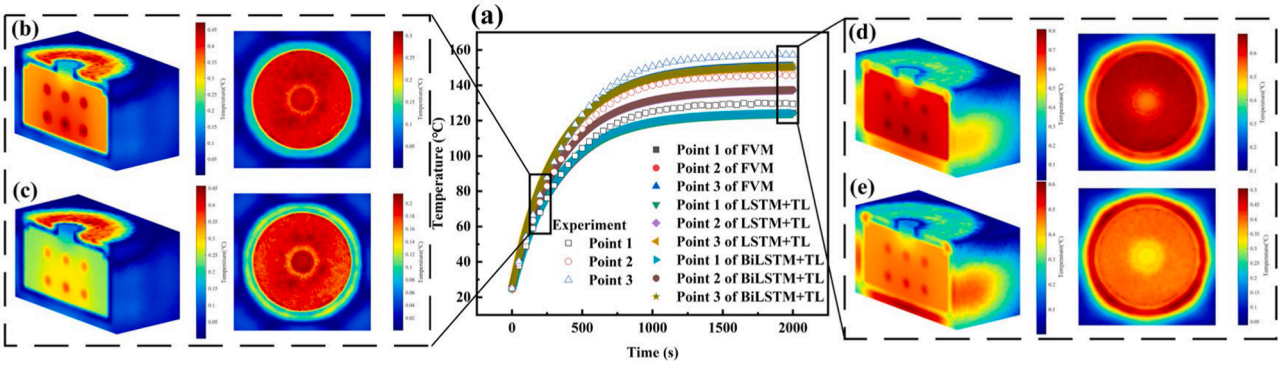

Fig. 9. The predicted temperature based on LSTM+TL and BiLSTM+TL. (a) The experiment and simulation temperature of three critical points versus time. (b) The temperature error of LSTM+TL at 200 s. (c) The temperature error of BiLSTM+TL at 200 s. (d) The temperature error of LSTM+TL at 2000 s. (e) The temperature error of BiLSTM+TL at 2000 s.

Nevertheless, the electronics is a temperature-sensitive object, and temperature distribution across the entire object is critical for ensuring proper system functionality. Therefore, we have selected the temperature fields of two critical cross sections (Fig. 3(c)) for further analysis.

According to the temperature curves in Fig. 8(a) and Fig. 9(a), two important stages are highlighted for analysis in the temperature rising stage and stabilization stage, namely at the time of 200 s and 2000 s. The former stage is in the steepest part of the temperature rise curve and the latter stage is in the flattest part of the temperature rise curve. The two stages correspond to the two most important stages in the operation of an electronic system, namely power surge in short time and smooth operation for long time. As shown in Fig. 8(b-e) and Fig. 9(b-e), the BiLSTM and BiLSTM+TL both have better prediction performance than LSTM and LSTM+TL accordingly. The temperature errors tend to be greater in regions with high temperatures. At 200 s, the temperature of the electronic system is low, so the error is concentrated on the copper block. As the temperature continues to rise, the heat gradually spreads outwards and the temperature of the shell becomes distorted at 2000 s.

As shown in Table 1, the thermophysical parameters are material dependent and the difference is significant, especially the thermal conductivity, which is required by the spray cooling heat module. Heat will travel and accumulate in the direction of least thermal resistance. It can be learned from Fig. 7 that the temperature error is greater in the high temperature region due to the fact that the thermal behaviors is more complex with more non-linear factors such as heat leakage and thermal radiation compared to other regions. Therefore, it is more difficult to calculate the temperature field accurately in the high temperature region. However, for the critical temperature measurement points, all four methods have good prediction results, and the error can be controlled within 0.1 °C. In the low-temperature region, the maximum temperature error is about 0.45 °C, and in the high-temperature region, it is about 0.5 °C. Machine learning has shown great ability to predict POD mode coefficients and thus temperature fields, and the accuracy of the algorithm

Table 1
Thermophysical parameters of materials used in the simulation.

	Materials	Thermal conductivity (W/m·K)	Density (kg/m^3)	Specific heat capacity (J/kg·K)
PEEK	PEEK	0.29	1400	1800
Copper block	Copper	398	8930	386
Thermal insulation cotton	Cotton	0.03	80	1220
Heating rods	Al_2O_3	30	3960	850

Table 2
Setup of the spray cooling cases.

No.	Parameters			
	Spray volumetric flux (mL/min)	Nozzle-to-surface distance (mm)	Coolant inlet temperature (°C)	Power (W)
O	100	10	25	550
A	100	10	25	750
B	150	10	25	550
C	150	10	25	800
D	100	20	25	600
E	100	30	25	600
F	100	10	15	600
G	100	10	35	600

optimized by TL has been slightly improved.

3.4. The computational accuracy and cost of different cases

The above sections demonstrate the validity of the machine learning through the results of the temperature field calculations for case O, but only for the dataset of the first five POD modes. To further verify the broader applicability of these conclusions, the four methods are conducted to predict ten mode coefficients based on eight working conditions, creating a total of 320 neural networks. The POD mode coefficients are the dataset for machine learning and the most important parameter for reconstructing the temperature field. The RMSE and R^2 results of POD mode coefficients are shown in Fig. 10 based on four methods. The four methods present excellent prediction accuracy in each POD mode coefficient and the maximum RMSE is less than 0.1. The RMSE values generally follow a trend of initially increasing and then decreasing with the order of the mode coefficients, peaking around the seventh and eighth modes. As illustrated in Fig. 6, the turning trend is due to the fact that the pattern of change of mode coefficients over time is more nonlinear at higher order POD mode. However, better prediction results are achieved with the ninth and tenth modes, which is due to the decrease in the extreme values. The R^2 is suitable for comparing the performance of the different models compared to RMSE, and in line with the previous discussion, the four methods show good prediction ability in the first five POD modes. However, in the high order modes, large errors are observed. The smallest R^2 reaches 0.416, mainly due to the data noisy and non-linear relationships. Notably, the introduction of TL effectively improves R^2, both for LSTM and BiLSTM. It can be seen that the prediction results of machine learning are affected by a variety of factors and need to be comprehensively evaluated. The same conclusions as above can be drawn between the different methods, with BiLSTM outperforming LSTM, and the introduction of TL leading to overall better results than without TL. Among the four methods, BiLSTM+TL delivers the best overall prediction results.

A very important conclusion can be drawn from the above analysis that the prediction of LSTM are already very effective and the reduction of computational error by BiLSTM or TL is limited. This brings us to an important evaluation criterion for our algorithm, namely the cost of computational resources. High computational accuracy and low time-consumption are often difficult to satisfy simultaneously. Fig. 11 presents the computational time for different methods including training time and prediction time. If all solutions are computed using FVM, the

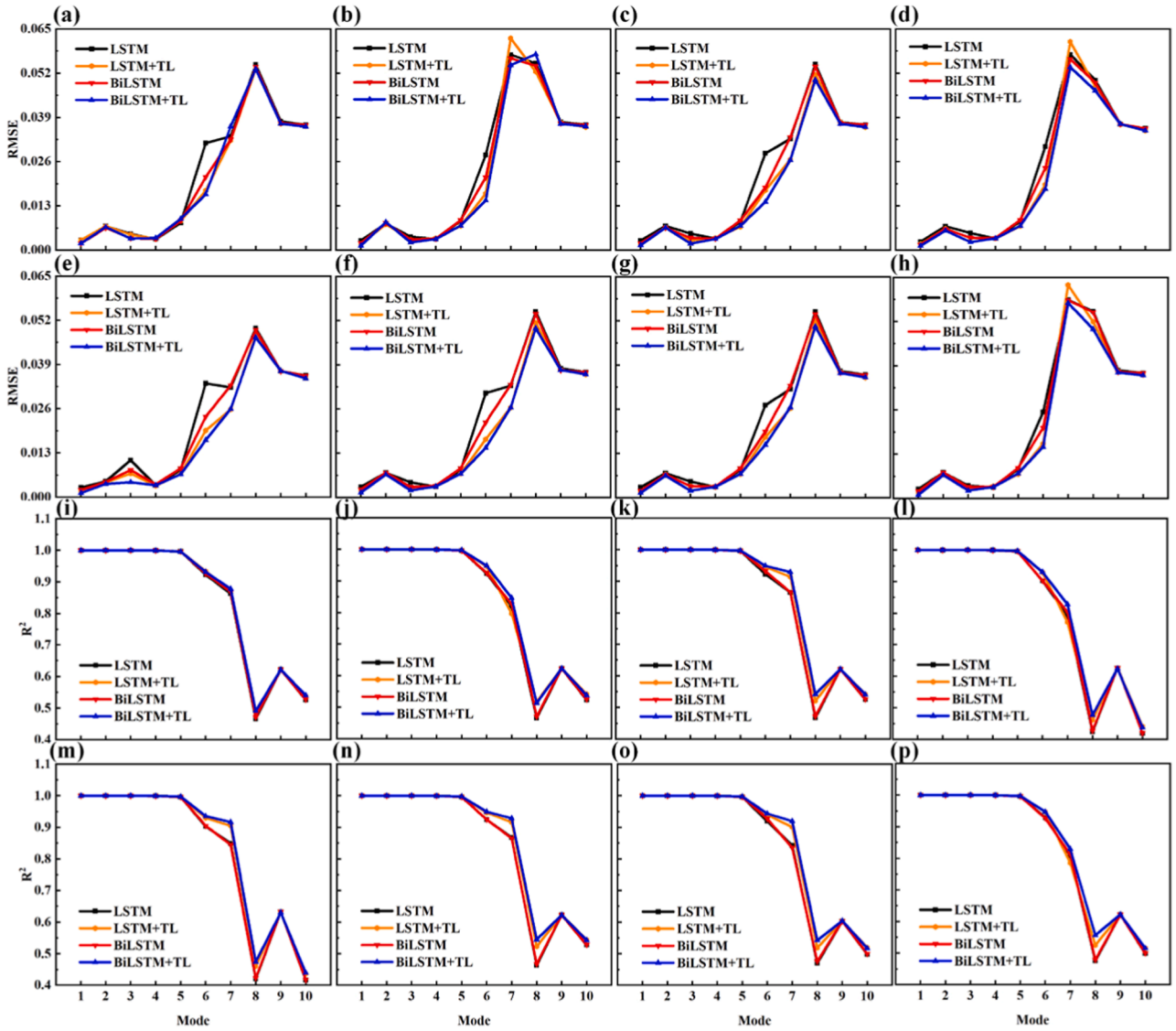

Fig. 10. The RMSE and R^2 for each POD mode coefficient of different cases. (a) and (i): Case O. (b) and (j): Case A. (c) and (k): Case B. (d) and (l): Case C. (e) and (m): Case D. (f) and (n): Case E. (g) and (o): Case F. (h) and (p): Case G.

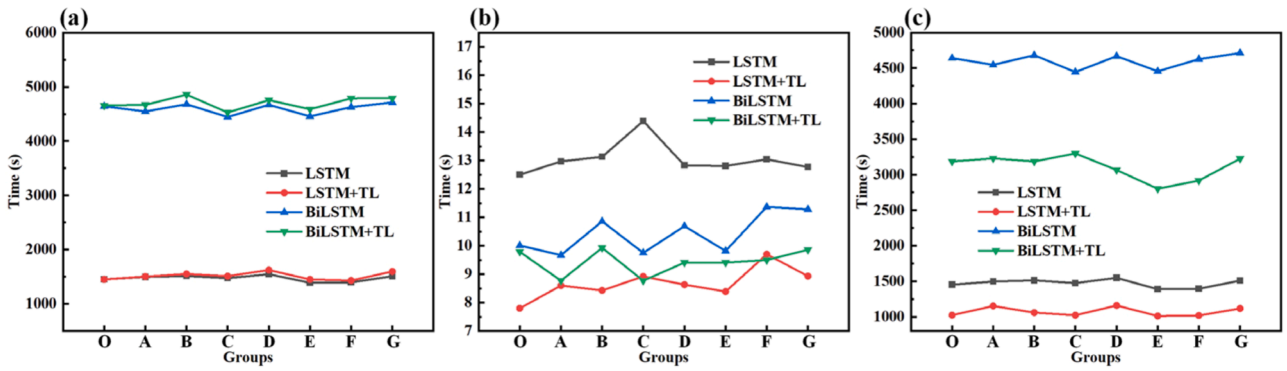

Fig. 11. The computational time for different methods. (a) The training time based on same time steps. (b) The prediction time. (c) The training time based on same RMSE.

average time required for the 0–2000 s temperature field calculation of different cases is 47,684 s. As for case O, the saved time is 22,371 s based on POD-LSTM and the proposed framework saves 46.9 % of the calculation time. The time savings mainly come from the extrapolation of the temperature field of 1001–2000 s, where the temperature field calculation can rely on our algorithm instead of the time-consuming FVM. The BiLSTM takes on average 4597 s for training the dataset, which is 3.12 times longer than LSTM due to bidirectional traversal. As shown in Fig. 11(a), it is essentially the same for different cases, and there are 300 iterations. With the addition of TL, the training time remains almost unchanged. After the neural network is built, the time spent on prediction is also crucial for the efficiency of the computation. Fig. 11(b) demonstrates that algorithms incorporating TL are substantially more efficient than those without it. The LSTM+TL saves 38 % time with a minimum prediction time of only 7.8 s compared to LSTM. The BiLSTM+TL saves 16.5 % time with a minimum prediction time of only 8.77 s compared to BiLSTM. The prediction efficiency is also improved in BiLSTM compared to LSTM, with the maximum lift of 32.2 %. Fig. 11 (c) further highlights the advantages of TL under the same RMSE criterion. It can be found that the training time is greatly reduced for the algorithms containing TL, with a maximum reduction of 30.7 % in the computation time of LSTM and a minimum of only 1012 s. The computation time of BiLSTM is reduced by a maximum of 37.1 %, with a minimum of only 2803 s. These results underscore that, for temperature field prediction, the inclusion of TL offers substantial savings in computational resources, making it a highly effective optimization strategy. What's more, both CET and CDT show excellent computational results, and the type of dataset should be the main consideration in applications.

For a more intuitive and comprehensive comparison of the different methods, we list the key parameters in Table 3. The temperatures and POD mode coefficients are compared with the experiment and FVM results and ten POD mode coefficients are analyzed. The findings demonstrate that the presented framework successfully captures the dominant thermal field characteristics while achieving a significant reduction in computational costs comparing with full-order methods. It should be noted, however, that optimal mode selection requires strategic optimization based on specific engineering applications.

4. Conclusion

Ultra-fast simulation has become indispensable in the AI era, especially for the high-heat-flux electronic systems. As emerging approaches to superfast simulation, POD and machine learning are both famous data-driven methods which have their pros and cons. In this work, we innovatively integrate POD and machine learning to achieve dual acceleration for temperature field simulation. The POD mode coefficients are predicted by utilizing the predictive power of machine learning on nonlinear problems, thereby circumventing the instability, complex meshing, and computational iterations associated with traditional GP methods. For prediction on time scales, we validate the applicability of both LSTM and BiLSTM methods, and introduce TL to strike a balance between computational accuracy and efficiency.

The results demonstrate the feasibility of our proposed algorithmic framework, and the effect of the POD mode coefficients on the temperature field is analyzed. From there, four machine learning methods are targeted and tested, showing excellent agreement with both experiments and FVM. The computational accuracy and efficiency are greatly improved, for the standard case O, the maximum temperature error is 6.52 %. For ten mode coefficients of eight working conditions, the maximum RMSE is less than 0.1. Through the introduction of TL, computation time is saved significantly, with the lowest training time of 1012 s and the lowest prediction time of 7.8 s. This is a qualitative leap compared to the calculation time of days in the past. The combination of POD and machine learning shows remarkable capability, which provides a brand-new idea for the fast simulation of complex physical problems. In the future, the algorithm can be further enhanced for problems coupled with different physical fields, especially in application scenarios that require the high result refinement. Such advancements will drive transformative progress in energy systems, ecological protection, and intelligent manufacturing, paving the way for innovative solutions in these critical domains.

CRediT authorship contribution statement

Linyi Xiang: Writing – original draft, Validation, Software, Methodology, Investigation, Formal analysis, Data curation, Conceptualization. **Fengjun Wang:** Validation, Methodology, Investigation, Formal

Table 3
Performance of different methods.

Methods	Maximum temperature error (°C)	Average temperature error (°C)	Average calculation time (s)	RMSE of POD mode coefficient	R^2 of POD mode coefficient
LSTM	9.570	5.582	1472	0.0584	0.416
LSTM+TL	9.586	5.589	1070	0.0628	0.436
BiLSTM	9.398	5.489	4597	0.0583	0.417
BiLSTM+TL	9.402	5.492	3114	0.0573	0.438

analysis, Conceptualization. **Yuntao Zha:** Software, Methodology, Data curation, Conceptualization. **Yupeng Hu:** Methodology, Investigation, Conceptualization. **Bisheng Zhang:** Software, Resources, Investigation. **Xuan Yang:** Validation, Resources, Investigation. **Run Hu:** Writing – review & editing, Supervision, Resources. **Xiaobing Luo:** Writing – review & editing, Supervision, Resources, Funding acquisition.

Declaration of competing interest

The authors declare that they have no known competing financial interests or personal relationships that could have appeared to influence the work reported in this paper.

Acknowledgments

The authors acknowledge the financial support from National Key R & D Project from Ministry of Science and Technology of China (2022YFA1203100), National Natural Science Foundation of China (52422603, 52076087, 5221150005), and Natural Science Foundation of Hubei Province (2023AFA072).

Data availability

Data will be made available on request.

References

[1] R. Van Erp, R. Soleimanzadeh, L. Nela, et al., Co-designing electronics with microfluidics for more sustainable cooling, Nature 585 (2020) 211–216.
[2] X. Luo, R. Hu, S. Liu, et al., Heat and fluid flow in high-power LED packaging and applications, Prog. Energy Combust. Sci. 56 (2016) 1–32.
[3] L. Xiang, et al., High-performance thermal management system for high-power LEDs based on double-nozzle spray cooling, Appl. Therm. Eng. 231 (2023) 121005.
[4] B. Agostini, M. Fabbri, J.E. Park, et al., State of the art of high heat flux cooling technologies, Heat Transf. Eng. 28 (2007) 258–281.
[5] L. Xiang, R. Hu, Liquid directional steering, Matter. 5 (2022) 13–15.
[6] S. Basu, K.S. Hariharan, S.M. Kolake, et al., Coupled electrochemical thermal modelling of a novel Li-ion battery pack thermal management system, Appl. Energ. 181 (2016) 1–13.
[7] L. Xiang, et al., Performance of spray cooling with vertical surface orientation: an experimental investigation, Appl. Therm. Eng. 219 (2023) 119434.
[8] A. Untrau, S. Sochard, F. Marias, et al., A fast and accurate 1-dimensional model for dynamic simulation and optimization of a stratified thermal energy storage, Appl. Energ. 333 (2023) 120614.
[9] S.V Patankar, Airflow and cooling in data center, J. Heat Trans. T ASME 132 (2010) 073001.
[10] K. Lu, et al., A review of model order reduction methods for large-scale structure systems, Shock Vib. 2021 (2021) 1–19.
[11] M.I. Jordan, T.M. Mitchell, Machine learning: trends, perspectives, and prospects, Science 349 (2015) 255–260.
[12] R. Swischuk, L. Mainini, B. Peherstorfer, et al., Projection-based model reduction: formulations for physics-based machine learning, Comput. Fluids. 179 (2019) 704–717.
[13] M. Bergmann, L. Cordier, J.P. Brancher, Optimal rotary control of the cylinder wake using proper orthogonal decomposition reduced-order model, Phys. Fluids 17 (2005) 097101.
[14] M.A. Nikolaidis, P.J. Ioannou, B.F. Farrell, et al., POD-based study of turbulent plane Poiseuille flow: comparing structure and dynamics between quasi-linear simulations and DNS, J. Fluid. Mech. 962 (2023) A16.
[15] J. Bailon-Cuba, M.S. Emran, J. Schumacher, Aspect ratio dependence of heat transfer and large-scale flow in turbulent convection, J. Fluid. Mech. 655 (2010) 152–173.
[16] P. Ding, X.H. Wu, Y.L. He, et al., A fast and efficient method for predicting fluid flow and heat transfer problems, J. Heat Trans.T ASME 130 (2008) 032502.
[17] V.K.R. Vuppula, M. Ramanujam, V. Runkana, Reduced-order modeling of conjugate heat transfer in lithium-ion batteries, Int. J. Heat Mass Trans. 227 (2024) 125537.
[18] Z. Luo, F. Teng, J. Chen, A POD-based reduced-order Crank–Nicolson finite volume element extrapolating algorithm for 2D Sobolev equations, Math. Comput. Simul. 146 (2018) 118–133.
[19] D. Rempfer, On low-dimensional Galerkin models for fluid flow, Theor. Comp. Fluid Dyn. 14 (2000) 75–88.
[20] M.J. Balajewicz, E.H. Dowell, B.R Noack, Low-dimensional modelling of high-Reynolds-number shear flows incorporating constraints from the Navier–Stokes equation, J. Fluid. Mech. 729 (2013) 285–308.
[21] T. Murata, K. Fukami, K. Fukagata, Nonlinear mode decomposition with convolutional neural networks for fluid dynamics, J. Fluid. Mech. 882 (2020) A13.
[22] M.F. Barone, I. Kalashnikova, D.J. Segalman, et al., Stable Galerkin reduced order models for linearized compressible flow, J. Comput. Phys. 228 (2009) 1932–1946.
[23] M. Milano, P. Koumoutsakos, Neural network modeling for near wall turbulent flow, J. Comput. Phys. 182 (2002) 1–26.
[24] Z. Chua Khoo, C.H. Chan, Y. Hwang, A sparse optimal closure for a reduced-order model of wall-bounded turbulence, J. Fluid. Mech. 939 (2022) A11.
[25] C. Yu, Y. Li, Q. Chen, et al., Matrix-based wavelet transformation embedded in recurrent neural networks for wind speed prediction, Appl. Energ. 324 (2022) 119692.
[26] K. He, X. Zhang, S. Ren, et al., Deep residual learning for image recognition, in: 2016 IEEE Conference on Computer Vision and Pattern Recognition (CVPR), 2016, pp. 770–778.
[27] W. Xi, Y.J. Lee, et al., Ultrahigh-efficient material informatics inverse design of thermal metamaterials for visible-infrared-compatible camouflage, Nat. Comm. 14 (2023) 4694.
[28] N. Omata, S. Shirayama, A novel method of low-dimensional representation for temporal behavior of flow fields using deep autoencoder, AIP. Adv. 9 (2019) 015006.
[29] A. Güemes, S. Discetti, A. Ianiro, Sensing the turbulent large-scale motions with their wall signature, Phys. Fluids 31 (2019) 125112.
[30] M. Schuster, K.K Paliwal, Bidirectional recurrent neural networks, IEEE T Signal. Proces. 45 (1997) 2673–2681.
[31] M.N. Fekri, H. Patel, K. Grolinger, et al., Deep learning for load forecasting with smart meter data: online adaptive recurrent neural network, Appl. Energ. 282 (2021) 116177.
[32] S. Li, W. Li, C. Cook, et al., Independently Recurrent Neural Network (IndRNN): building a longer and deeper RNN, in: 2018 IEEE/CVF Conference on Computer Vision and Pattern Recognition (CVPR), 2018, pp. 5457–5466.
[33] Shi X., Chen Z., Wang H., et al. Convolutional LSTM network: a machine learning approach for precipitation nowcasting. arXiv preprint 2015.
[34] A. Rahman, V. Srikumar, A.D Smith, Predicting electricity consumption for commercial and residential buildings using deep recurrent neural networks, Appl. Energ. 212 (2018) 372–385.
[35] W. Kong, Z.Y. Dong, Y. Jia, et al., Short-term residential load forecasting based on LSTM recurrent neural network, IEEE T Smart Grid 10 (2019) 841–851.
[36] K. Cao, T. Zhang, J. Huang, Advanced hybrid LSTM-transformer architecture for real-time multi-task prediction in engineering systems, Sci. Rep. 14 (2024) 4890.
[37] S. Siami-Namini, N. Tavakoli, A.S Namin, The performance of LSTM and BiLSTM in forecasting time series, in: 2019 IEEE International Conference on Big Data (Big Data), 2019, pp. 3285–3292.
[38] T. Peng, C. Zhang, J. Zhou, et al., An integrated framework of Bi-directional long-short term memory (BiLSTM) based on sine cosine algorithm for hourly solar radiation forecasting, Energy 221 (2021) 119887.
[39] O. San, R. Maulik, Extreme learning machine for reduced order modeling of turbulent geophysical flows, Phys. Rev. E 97 (2018) 042322.
[40] Z. Wang, D. Xiao, F. Fang, et al., Model identification of reduced order fluid dynamics systems using deep learning, Int. J. Numer. Meth. Fl. 86 (2018) 255–268.
[41] M.Z. Yousif, H.C. Lim, Reduced-order modeling for turbulent wake of a finite wall-mounted square cylinder based on artificial neural network, Phys. Fluids 34 (2022) 015116.
[42] Mohan A.T., Gaitonde D.V. A deep learning based approach to reduced order modeling for turbulent flow control using LSTM neural networks. arXiv preprint 2018.
[43] L. Xiang, B. Zhang, Y. Zha, et al., Physics-Informed proper orthogonal decomposition for accurate and superfast prediction of thermal field, ASME J. Heat Mass Transf. 147 (7) (2025) 073301.